



1 **Retrieval and analysis of the composition of an aerosol mixture through Mie-Raman-**
2 **Fluorescence lidar observations.**

3

4 Igor Veselovskii¹, Boris Barchunov¹, Qiaoyun Hu², Philippe Goloub², Thierry Podvin², Mikhail
5 Korenskii¹, Gaël Dubois², William Boissiere², Nikita Kasianik¹

6

7 ¹*Prokhorov General Physics Institute of the Russian Academy of Sciences, Moscow, Russia.*

8 ²*Univ. Lille, CNRS, UMR 8518 - LOA - Laboratoire d'Optique Atmosphérique, F-59650 Lille,*
9 *France*

10 **Correspondence:** Philippe Goloub (philippe.goloub@univ-lille.fr)

11

12 **Abstract**

13 In the atmosphere, aerosols can originate from numerous sources, leading to the mixing of different
14 particle types. This paper introduces an approach to the partitioning of aerosol mixtures in terms
15 of backscattering coefficients. The method utilizes data collected from the Mie-Raman-
16 fluorescence lidar, with the primary input information being the aerosol backscattering coefficient,
17 particle depolarization ratio (δ), and fluorescence capacity (G_F). The fluorescence capacity is
18 defined as the ratio of the fluorescence backscattering coefficient to the particle backscattering
19 coefficient at the laser wavelength. By solving a system of equations that model these three
20 properties (β_F , δ and G_F), it is possible to characterize a three-component aerosol mixture.
21 Specifically, the paper assesses the contributions of smoke, urban, and dust aerosols to the overall
22 backscattering coefficient at 532 nm. It is important to note that aerosol properties (δ and G_F) may
23 exhibit variations even within a specified aerosol type. To estimate the associated uncertainty, we
24 employ the Monte Carlo technique, which assumes that G_F and δ are random values uniformly
25 distributed within predefined intervals. In each Monte Carlo run, a solution is obtained. Rather
26 than relying on a singular solution, an average is computed across the whole set of solutions, and
27 their dispersion serves as a metric for method uncertainty. This methodology was tested using
28 observations conducted at the ATOLL observatory, Laboratoire d'Optique Atmosphérique,
29 University of Lille, France.

30

31 **1. Introduction**



32 Studying the physicochemical properties of atmospheric aerosols is crucial for
33 understanding their impact on Earth's radiation balance and climate. To simplify the complexity
34 of aerosol composition, it is essential to classify aerosol types. Categorization of aerosols into
35 several basic types, e.g. urban, dust, marine, biomass burning (Dubovik et al., 2002), allows to
36 cover the range of variability of observed aerosol parameters and facilitates the analysis and
37 interpretation of aerosol data. The multiwavelength Mie-Raman and HSRL (High Spectral
38 Resolution Lidar) lidar systems provide an unique opportunity to derive height-resolved particle
39 intensive properties, such as Angstrom exponents, lidar ratios, and depolarization ratios at multiple
40 wavelengths. These properties can be used as inputs for classification schemes (Burton et al., 2012,
41 2013; Groß et al., 2013; Mamouri et al., 2017; Papagiannopoulos et al., 2018; Nicolae et al., 2018;
42 Hara et al., 2018; Voudouri et al., 2019; Wang et al., 2021; Mylonaki et al., 2021; Wandinger et
43 al., 2023; Floutsi et al., 2023b). However, aerosols in the atmosphere often originate from multiple
44 sources, leading to the mixing of different particle types. To understand the impact of different
45 aerosol types within a mixture, it is necessary to quantify the content of each type.

46 In the cases involving mixtures of two aerosol types with significantly different
47 depolarization ratios, the partitioning of aerosol backscattering coefficients becomes
48 straightforward (Sugimoto and Lee, 2006; Tesche et al., 2009; Miffre et al., 2020). Burton et al.
49 (2014) have formulated the mixing rules for several aerosol intensive parameters, such as lidar
50 ratio, backscatter color ratio, depolarization ratio, and applied these rules to two-component
51 aerosol mixtures. However, the partition becomes increasingly challenging when dealing with
52 more than two types of particles. The limited number of lidar-measured intensive particle
53 properties specific to individual aerosol types contributes to this challenge. Even for a single
54 aerosol type, the measured particle parameters, such as lidar ratios, demonstrate a wide range of
55 variability (Floutsi et al., 2023a). Distinguishing between urban and smoke particles poses a
56 particular challenge as these two types exhibit similar lidar-measured properties (Floutsi et al.,
57 2023a). Therefore, additional independent information is needed to enhance the characterization
58 of aerosol parameters.

59 Independent information about aerosol properties can be obtained through fluorescence lidar
60 measurements (Reichardt et al., 2018, 2023; Veselovskii et al., 2020; Zhang et al., 2021). The
61 fluorescence lidar allows evaluating the fluorescence backscattering coefficient β_F , which is
62 derived from the ratio of fluorescence and nitrogen Raman backscatters (Veselovskii et al., 2020).



63 The particle intensive property in fluorescence lidar measurements is the fluorescence capacity
64 G_F , which is the ratio of β_F to the aerosol backscattering coefficient at the laser wavelength. The
65 fluorescence capacity of smoke is approximately one order higher than that of urban particles,
66 providing a basis for distinguishing between these two aerosol types (Veselovskii et al., 2022).
67 Additionally, recent studies have shown that a classification scheme relying on two intensive
68 parameters - the particle depolarization ratio at 532 nm (δ_{532}) and the fluorescence capacity,
69 effectively separates four aerosol types: dust, smoke, pollen, and urban (Veselovskii et al., 2022).
70 It is noteworthy that the current classification scheme does not discriminate particles based on their
71 absorption properties, so the "urban" type encompasses both continental aerosol and anthropogenic
72 pollution. Furthermore, maritime aerosol is not included in the classification at present, as the lidar
73 observations were performed over Lille, where maritime particles are not prevalent (though the
74 possibility of its inclusion is acknowledged).

75 In this study, we extended the approach beyond classification to partition aerosol mixtures
76 in terms of the backscattering coefficients of basic aerosol types. To test the approach, we analyzed
77 observations at the ATOLL (ATmospheric Observation at liLLe) at Laboratoire d'Optique
78 Atmosphérique, University of Lille, between 2020 and 2023, performed during periods of strong
79 smoke and dust episodes. We begin by providing a description of the lidar system and the approach
80 for mixture partition in Section 2. In the first part of the results section (Section 3.1), we present
81 two case studies that demonstrate how the algorithm operates. In the second part (Section 3.2), we
82 analyze the results obtained during the heatwave in July 2022. The paper concludes with a
83 summary of our findings in the conclusion section.

84

85 **2. Experimental setup and approach to aerosol mixture partition**

86 **2.1. Lidar system.**

87 The Mie-Raman-fluorescence lidar LILAS (Lille Lidar AtmosphereS) is equipped with a
88 tripled Nd:YAG laser that operates at a repetition rate of 20 Hz and has a pulse energy of
89 approximately 100 mJ at 355 nm. A 40 cm aperture Newtonian telescope is utilized to collect the
90 backscattered light, and Licel transient recorders with a range resolution of 7.5 m are employed to
91 digitize the lidar signals. This configuration allows for simultaneous detection in both analog and
92 photon counting modes. The objective of the LILAS system is to detect elastic and Raman
93 backscattering, which enables the measurement of various properties through the $3\beta+2\alpha+3\delta$ data



94 configuration. This includes three particle backscattering coefficients (β_{355} , β_{532} , β_{1064}), two
95 extinction coefficients (α_{355} , α_{532}), and three particle depolarization ratios (δ_{355} , δ_{532} , δ_{1064}). The
96 particle depolarization ratio, determined as a ratio of cross- and co-polarized components of the
97 particle backscattering coefficient, was calculated and calibrated in the same way as described in
98 Freudenthaler et al. (2009). Additionally, the LILAS system is capable of profiling the laser-
99 induced fluorescence of aerosol particles. This is achieved by using a wideband interference filter
100 with a width of 44 nm, centered at 466 nm, as suggested by Veselovskii et al. (2020). Due to the
101 strong sunlight background during daytime, the fluorescence observations are limited to nighttime
102 hours.

103 The calculation of the fluorescence capacity G_F can be performed using backscattering
104 coefficients at any laser wavelength. In our study, we specifically used β_{532} , as it is determined
105 using rotational Raman scattering and is considered to be the most reliable, thus $G_F = \frac{\beta_F}{\beta_{532}}$. To
106 supplement our measurements, additional information about atmospheric properties was obtained
107 from radiosonde measurements conducted at Herstmonceux (UK) and Beauvechain (Belgium)
108 stations, which are located approximately 160 km and 80 km away from the observation site,
109 respectively. The lidar measurements were primarily conducted vertically. In cases where
110 observations were made at an angle to the horizon, the corresponding information has been
111 included in the captions of the figures.

112

113 2.2. Approach for the mixture partition

114 The lidar system measures up to nine independent properties of aerosols. However, our
115 main focus is on separation the backscatters of individual aerosol types with high spatiotemporal
116 resolution. To calculate parameters related to the extinction coefficient, such as lidar ratio or
117 extinction Angstrom exponent, it is necessary to average lidar profiles over a substantial
118 spatiotemporal interval. In this study, as a first step, we use two parameters with high resolution
119 in both height and temporal domains: the depolarization ratio δ_{532} and the fluorescence capacity
120 G_F . Moreover, the calculation process partially cancels out the overlap functions, allowing us to
121 derive δ_{532} and G_F closer to the ground compared to aerosol extinction. We are considering a
122 scenario where only three externally mixed aerosol types occur, such as smoke (s), dust (d), and



123 urban (u). The aerosol and fluorescence backscattering coefficients (β_{532} and β_F) are the sum of
 124 their respective contributions.

$$125 \quad \beta_{532} = \beta_{532}^s + \beta_{532}^d + \beta_{532}^u \quad (1)$$

$$126 \quad \beta_F = \beta_F^s + \beta_F^d + \beta_F^u \quad (2)$$

127 The fluorescence capacities for each aerosol type are:

$$128 \quad G_F^i = \frac{\beta_F^i}{\beta_{532}^i} \quad (3)$$

129 where $i = s, d, u$. The fractions of β_{532} for individual aerosol types are:

$$130 \quad \eta_i = \frac{\beta_{532}^i}{\beta_{532}} \quad (4)$$

131 By definition:

$$132 \quad \eta_s + \eta_d + \eta_u = 1. \quad (5)$$

133 The fluorescence capacity can be expressed as a linear combination of the fluorescence
 134 capacities of each aerosol type, as shown in Eq. 6:

$$135 \quad G_F = \eta_s G_F^s + \eta_d G_F^d + \eta_u G_F^u \quad (6)$$

136 The particle depolarization ratio is a ratio of the cross- and co-polarized component of the
 137 backscattering coefficient: $\delta_{532} = \frac{\beta_{532}^\perp}{\beta_{532}^\parallel}$. However, for the mixture analysis, the use of the

138 depolarization potential $\delta'_{532} = \frac{\delta_{532}}{1 + \delta_{532}}$ is preferable, because δ' , the same as G_F , is a linear

139 combination of the depolarization potentials of individual particle types ($\delta'_{532}^s, \delta'_{532}^d, \delta'_{532}^u$), as outlined
 140 by Burton et al. (2014).

$$141 \quad \delta'_{532} = \eta_s \delta'_{532}^s + \eta_d \delta'_{532}^d + \eta_u \delta'_{532}^u \quad (7)$$

142 Finally, we have a system of three equations (5-7) from which we can determine the relative
 143 contributions of each aerosol type by finding η_s, η_d and η_u . In our study, we solve the system (Eq.
 144 5-7) using the least squares method with an additional constraint on the non-negativity of solutions.
 145 To achieve equal weighting of Eq.6 and 7, each equation is scaled by a factor so that the Euclidean
 146 norm of the coefficients G_F^s, G_F^d, G_F^u and $\delta'_{532}^s, \delta'_{532}^d, \delta'_{532}^u$ (considered as a 3-element vectors) become
 147 equal to 1. As mentioned earlier, the particle parameters may vary within predetermined ranges,



148 even for a specific aerosol type. However, the exact values of G_F^i and δ_{532}^i at a specific height/time
149 pixel are unknown. To address the uncertainty in η_i , we employ the Monte Carlo technique,
150 assuming that G_F^i and δ_{532}^i are random values uniformly distributed within the predetermined
151 intervals. For each Monte Carlo trial, random values of G_F^i and δ_{532}^i are generated. Instead of
152 relying on a single solution, we conduct a series of Monte Carlo trials in order to obtain a set of
153 solutions and calculate the average of this set. The dispersion of these solutions is taken as a
154 measure of method uncertainty. The number of Monte Carlo trials was set to 100 and further
155 increase in this number did not significantly impact either the final average or the dispersion of
156 solutions. In our classification scheme, we include four types of aerosols (smoke, pollen, urban,
157 dust). Nevertheless, the system of equations (Eq. 5-7) consists of only three equations. Given that
158 it is highly unlikely to have all four aerosol types coexisting at a single height/time pixel, one of
159 the four types can be excluded a priori based on a G_F - δ_{532} diagram or other pertinent
160 considerations. Another option is to exclude one aerosol type at each height/time pixel based on
161 the lidar data itself, as described below. Such method we will call Automatic Type Selection (ATS)
162 For ATS, we solve the system Eq. 5-7 for the triplets (S, P, U) , (S, P, D) , (S, D, U) , and $(P,$
163 $D, U)$, where S, D, U, P denote Smoke, Dust, Urban, Pollen, respectively. To determine which
164 aerosol types can be excluded, we use the discrepancy for Eq. 6 and 7 as a criterion. Specifically,
165 we calculate the difference between the input data (G_F - δ_{532}) and the corresponding values obtained
166 by substituting the solution into the right-hand side of Eq. 6 and 7. These two differences are
167 treated as a 2-element vector, and the Euclidean norm of this vector is taken as the discrepancy.
168 The aerosol triplet that provides the least discrepancy is chosen for this single Monte Carlo trial
169 and for the height/time pixel. This procedure is repeated for every Monte Carlo trial, and after
170 averaging, the spatiotemporal distributions of η_s , η_p , η_u , and η_d are evaluated.

171

172 **3. Application of partition algorithm to lidar observations**

173 The uncertainty of the partitioning of backscattering coefficients depends on the range of
174 G_F and δ_{532} variations in each aerosol type. To establish this range, we analyzed measurement
175 sessions at the ATOLL for the period of 2020-2023. Our focus was on observation episodes
176 characterized by stable atmospheric conditions, where only a single aerosol type predominated, at
177 least within specific height/time intervals. Moreover, we took precautions to ensure that the



178 relative humidity in the selected intervals remained below 60% to minimize the impact of particle
179 hygroscopic growth. Based on the obtained results, we summarized the ranges of parameter
180 variation in Table 1. The depolarization ratios δ_{532} for smoke and urban particles fall within the
181 range of 2%-8%, while for dust, this range is 25%-35%. The depolarization ratio of long
182 transported dust can be lower, but at this stage, we do not consider possible modifications of dust
183 properties during transportation. We attribute lower values of δ_{532} to the mixing of dust with
184 pollutants (urban aerosol in our model). The fluorescence capacity of smoke in the upper
185 troposphere can be as high as 10×10^{-4} (Veselovskii et al., 2023), but below 8 km, it mainly falls
186 within the range of $(2.5-4.5) \times 10^{-4}$. For dust and urban particles, the values of fluorescence
187 capacities are within the intervals of $(0.05-0.45) \times 10^{-4}$ and $(0.2-0.8) \times 10^{-4}$, respectively.
188 Determining the ranges of δ_{532} and G_F for pollen is particularly challenging because, in the North
189 of France, pollen is commonly mixed with other aerosol types. Moreover, the depolarization of
190 pollen particles varies significantly from one type to another (Cao et al., 2010). In the Lille area,
191 one dominant taxon is birch (Veselovskii et al., 2021) with a depolarization ratio of δ_{532} at around
192 30% (Cholleton et al., 2022). In our analysis, the depolarization ratio is set within the 30%-40%
193 interval. The variation range of G_F is estimated from our measurements to be within $(1.0-2.5) \times 10^{-4}$.
194 4.

195 Table 1. Variation ranges of fluorescence capacity and the particle depolarization ratio for different
196 types of aerosols.

Type	$G_F, 10^{-4}$	$\delta_{532}, \%$
Smoke	2.5÷4.5	2.0÷8
Pollen	1÷2.5	30÷40
Urban	0.2÷0.8	2.0÷8
Dust	0.05÷0.45	25÷35

197

198 Below, we present two examples of applying the described approach to measurements performed
199 on March 27-28, 2022, and October 1-2, 2023.

200



201 **March 27-28, 2022**

202 The spatiotemporal distributions of the aerosol backscattering coefficient β_{532} , the particle
203 depolarization ratio δ_{532} , and the fluorescence capacity G_F on March 27-28, 2022, are shown in
204 Fig.1. Relative humidity decreased with height, ranging from 70% at 600 m to 55% at 1800 m.
205 Aerosols were primarily found below 2500 m, with several distinguishable particle types identified.
206 The particle depolarization ratio increased to 30% at 2000 m during the 20:00-22:00 UTC period,
207 indicating the presence of dust. Additionally, high values of the fluorescence capacity (up to
208 2.5×10^{-4}) for the 00:00-05:00 UTC period suggest the presence of smoke.

209 Fig.2a presents the G_F - δ_{532} diagram for these measurements. The red boxes represent the
210 parameter ranges used for aerosol classification, which are slightly broader than those outlined in
211 Table 1 to account for mixtures where one type is predominant. Dust, smoke, and urban particles
212 can be distinguished in the clusters of points on the diagram, with intervals indicating mixed
213 particle types. Although March is typically a pollen season in Lille, pollen particles did not
214 significantly contribute to the observed episode. Utilizing this classification scheme, we assess the
215 spatiotemporal distribution of aerosol types in Fig.2b, following the methodology outlined in
216 Veselovskii et al. (2022). Regions predominated by dust, smoke, and urban particles are clearly
217 identified. A small amount of pollen is observed towards the end of the session at approximately
218 700 m height. The grey color in Fig.2b represents aerosol mixtures where the particle type cannot
219 be definitively identified. The aerosol classification presented in Fig. 2b finds support in the results
220 of the HYSPLIT Backward Trajectory Analysis (Stein et al., 2015) depicted in Figure 3.
221 Specifically, the air masses below 1000 m height were transported over the Belgium, and the
222 presence of urban aerosol is expected. Conversely, the air masses above 1500 m were transported
223 over regions with extensive forest fires in Greece and near Spain, suggesting a potential mixture
224 of smoke and dust.

225 By applying the partition technique described in Sect.2.2, we can determine the contribution
226 of each particle type to the total backscattering coefficient β_{532} . The spatiotemporal distributions of
227 η_s , η_u , and η_d in Fig.4 were assessed assuming that pollen contribution can be neglected. The
228 algorithm operates smoothly, showing distributions without any unrealistic high-frequency
229 oscillations. By observing the distributions, it can be concluded that the smoke plume actually
230 contains a significant amount of urban aerosol, while the dust plume does not show the presence
231 of other particle types.



232 The distributions in Fig.4 represent the mean values of η_s , η_u , and η_d . To understand the
233 uncertainty caused by potential variations in particle characteristics, Fig.5 displays the vertical
234 profiles of η_s , η_u , and η_d for the period between 21:00-22:00 UTC, along with the corresponding
235 standard deviations. Urban particles are predominant below 1000 m with a deviation from the
236 mean value of roughly 5%. Above 1500 m, η_u decreases to 0.05 and the uncertainty increases to
237 100%. Conversely, dust can be disregarded below 1000 m, but becomes predominant above 1000
238 m. Smoke contribution during the considered time period is low and only becomes noticeable
239 ($\eta_s \sim 0.15$) in the 1250-1500 m range. As mentioned earlier, the results in Fig. 4 were obtained
240 without considering pollen. To assess the potential impact of pollen on the results, the partition
241 was carried out for four aerosol types using the ATS approach, as described in Section 2.2. The
242 corresponding profiles of $\eta_{s,4}$, $\eta_{u,4}$, and $\eta_{d,4}$ are depicted in Fig.5 with magenta lines. Notably, the
243 profiles obtained for three and four aerosol types are similar. Pollen does have some effect on
244 smoke contribution (η_s decreased from 0.14 to 1.0), but its influence on dust and urban particle
245 contribution is negligible.

246

247 **October 1-2, 2023**

248 Observations at ATOLL in 2023 were notable for frequent intensive smoke events. North
249 American wildfire smoke, transported over the Atlantic, was observed from mid-May until
250 October. In some autumn episodes, smoke descended from the troposphere to ground level. One
251 such episode is shown in Fig.6, which presents the spatiotemporal distributions of β_{532} , δ_{532} , and
252 G_F during the night of October 1-2, 2023. During this period, the relative humidity decreased with
253 height, from 50% at 500 m to 30% at 3500 m. Strong aerosol layers were observed up to 5 km in
254 height, and the depolarization ratio δ_{532} exceeded 25% above 2000 m, indicating the predominance
255 of dust. However, below 1000 m, a low depolarization ratio ($\delta_{532} < 8\%$) was accompanied by a
256 high fluorescence capacity of particles (up to 3.0×10^{-4}), identifying them as smoke. The G_F - δ_{532}
257 diagram in Fig.7a highlights the pixels attributed to dust, smoke, and urban particles. There are
258 also intervals where these types were mixed. These regions with mixed aerosols are represented
259 by the grey color in the distribution of particle types in Fig.7b. The results of aerosol classification
260 agree with HYSPLIT backward trajectories analysis. Fig.8 shows the five-days back trajectories
261 over Lille on October 2, 2023, at 00:00 UTC. The air masses over the Atlantic, containing North
262 American smoke, descend from 5000 m to the ground, leading to the predominance of smoke over



263 Lille at 500 m. The air masses at 1500 m are transported over the continent and may contain
264 pollutants, whereas the air masses at 2700 m arrive from Africa and are loaded with dust. Fig. 9
265 depicts the spatiotemporal distributions of η_s , η_u , η_d , derived in assumption that only three aerosol
266 types occur. Urban aerosol is localized primarily between the smoke and dust layers. Vertical
267 profiles of η_s , η_u , η_d for the 22:00-23:00 UTC period are presented in Fig.10. Smoke predominates
268 below 1000 m, with a smoke contribution ($\eta_s=0.7$ at 750 m) evaluated with an uncertainty of about
269 20%. The contribution of urban particles within the smoke layer (at 750 m) is $\eta_u=0.3$, with a
270 corresponding uncertainty of approximately 30%. Dust predominates above 2000 m ($\eta_d=0.8$), and
271 the uncertainty of η_d estimation is below 15%. Although the existence of pollen in October is quite
272 improbable, for testing purposes, we performed an inversion for four aerosol types using the ATS
273 method (magenta lines in Fig.10). The impact of including pollen is most pronounced for dust at
274 1750 m, where η_d is about 25% decreased. However, the values obtained still fall within the
275 estimated range of uncertainty. From the examples considered, we conclude that the contributions
276 of three aerosol components to the backscattering coefficient can be determined through joint
277 fluorescence and polarization measurements. The volume density, V_i , of i -th aerosol component
278 can be estimated from the backscattering coefficient using the corresponding lidar ratio, S_{532}^i , and
279 the extinction-to-volume conversion factors C_V^i (Mamouri and Ansmann, 2017; Ansmann et al.,
280 2019, 2021; He et al., 2023). Thus, for the i -th aerosol component:

$$281 \quad V_i = \beta_{532} \times \eta_i \times S_{532}^i \times C_V^i \quad (8)$$

282 The values of the conversion factors at 532 nm, derived from AERONET observations, along with
283 some reported lidar ratios, are summarized in Table 2. Therefore, the presented information allows
284 us to quantify the composition of the aerosol mixture.

285



286 Table 2. Lidar ratios (S_{532}^i) and extinction-to-volume conversion factors (C_V^i) for different types
287 of aerosol.

Type	Lidar ratio S_{532}^i , sr	C_V^i , $\mu\text{m}^3\text{cm}^{-3}/\text{Mm}^{-1}$
Urban	53-70 ⁵	0.3-0.41 ¹
Smoke (North American, aged)	55-73 ⁵	0.13 ³
Dust (North Africa)	40-50 ³	0.61-0.64 ¹ 0.67-0.73 ² 0.64-0.67 ⁴

288 ¹ Mamouri and Ansmann, 2017; ² Ansmann et al., 2019; ³ Ansmann et al., 2021; ⁴ He et al., 2023; ⁵ Burton et
289 al., 2013

290

291 4. Heatwave over Lille in July 2022.

292 The heatwave in France in July 2022 was attributed to a high-pressure system known as the
293 Azores High, which usually sits off Spain and pushed farther north, resulting in elevated
294 temperatures and multiple fires. The Sun photometer and lidar observations at ATOLL consistently
295 recorded an increase in aerosol content over Lille in the middle of July 2022. Fig.11 displays the
296 aerosol optical depth (AOD) at 500 nm and the Angstrom exponent for 380/500 nm wavelengths
297 provided by AERONET. Lidar observations were performed from July 16 to July 23, as shown in
298 the frame in Fig.10. Within this interval, the optical depth increased, reaching its peak on July 18.
299 The Angstrom exponent decreased, indicating the presence of dust. Fig.11 shows the column-
300 integrated particle volume, provided by AERONET, presented separately for the fine and coarse
301 mode particles. After July 16, the volume of the coarse mode increased approximately fourfold,
302 while the fine mode did not show significant changes, further supporting the presence of dust
303 particles. Unfortunately, volume retrievals are not available after July 20 due to the presence of
304 clouds. The methodology outlined in Sect. 2.2 was used to analyze the composition of aerosols
305 during the heatwave.

306 In Fig.13, we can see the spatiotemporal distributions of β_{532} , δ_{532} and G_F for four
307 measurement sessions between July 16 and July 23, 2022. On July 16-17, after midnight, a dust
308 layer with δ_{532} exceeding 20% appeared at a height of 5 km. The following night (July 17-18), the
309 lower boundary of the dust layer descended to 2 km. By the night of July 18-19, we observed



310 strong aerosol backscattering (above $1.0 \text{ Mm}^{-1}\text{sr}^{-1}$) from the ground up to a height of 5 km. Dust
311 was primarily found within two height ranges: 0.75-2.0 km and 3.0-5.0 km, where the particle
312 depolarization ratio δ_{532} exceeded 20%. The aerosol between these dust layers showed high
313 fluorescence capacity (above 2.0×10^{-4}), indicating the presence of smoke. Unfortunately, we could
314 not make long-term lidar observations from July 19-21 due to cloud cover. However, by the night
315 of July 22-23, we observed localized aerosols below 3 km. The values of δ_{532} and G_F were below
316 10% and 1.0×10^{-4} , respectively, which is typical for urban particles. The relative humidity during
317 the measurements for July 16-19 was below 60 % within the height range being considered. On
318 the night of July 22-23, the relative humidity was higher, reaching up to 80%. In Fig.14, we provide
319 the G_F - δ_{532} diagrams for the measurements shown in Fig.13. On the night of July 16-17, the
320 clusters corresponding to dust and smoke/urban particles are distinct. However, for July 17-19,
321 dust was mixed with smoke and urban particles, resulting in a characteristic pattern on the G_F - δ_{532}
322 diagram (Veselovskii et al., 2022). By the night of July 22-23, only one cluster, corresponding to
323 urban aerosol, was observed. The distributions of particle types in Fig.14 for the period of July 16-
324 19 contain extended gray regions where different types of particles are mixed and cannot be
325 identified. In Fig.15, we can see the partition technique used to evaluate the contributions of dust,
326 smoke, and urban aerosol to β_{532} . From this analysis, we can conclude that on the night of July 16-
327 17, the aerosol below 2.5 km was a mixture of smoke and urban particles, and the elevated dust
328 layer (00:00-03:00 UTC) contained a significant amount of urban particles (η_u is up to 0.4). On
329 July 18-19, the aerosol between the two dust layers, within the height range of 2-3 km, was also a
330 mixture of smoke and urban particles.

331 The aerosol classification based on fluorescence and depolarization measurements is
332 supported by the analysis of backward trajectories. Fig.16 shows the five-day backward
333 trajectories for four measurement sessions from Figure 15 at altitudes of 1500 m, 3000 m, and
334 4500 m. On July 16-17, the dust layer above 4000 m originates from North Africa, while smoke
335 at 3000 m is likely transported from North America. The air masses at 3000 m on July 17-18 are
336 transported from Africa over regions of wildfires in Spain, indicating a mixture of dust and smoke.
337 Smoke at 3000 m on July 18-19 again originates from wildfires in Spain, while the source of the
338 dust layers at 1500 m and 4000 m is in Africa. Finally, on July 22-23, the air masses arrive from
339 the West outside dust and smoke sources, and aerosol in Fig. 15 within the 1000-3000 m range is
340 identified as urban.



341 As mentioned, the volume density of each component can be estimated using Eq. 8. Fig.17
342 presents the vertical profiles of volume density for smoke, urban, and dust particles for four
343 measurement sessions from Fig.15. In the calculations, we used the mean values of η_s , η_u , η_d , as
344 well as the mean values of the lidar ratios and fluorescence capacity from Table 2. The lidar ratios
345 for smoke, urban, and dust are 64 sr, 61 sr, and 45 sr, respectively, and the fluorescence capacity
346 values are 0.13×10^{-4} , 0.35×10^{-4} , and 0.7×10^{-4} , respectively. The main contributors to the volume
347 are urban and dust particles, with smoke contributing noticeably only on July 18 and 19, but with
348 a volume density still below $5 \mu\text{m}^3\text{cm}^{-3}$. To assess the validity of our volume estimations, we
349 compared our results with AERONET retrievals. For this comparison, the volume profiles of each
350 component from Fig.17 were extrapolated to the ground, and the total column-integrated volume
351 was calculated. The results are depicted in Fig.12 by stars, with an additional measurement on July
352 19 (22:00-23:00) included. It is evident that the results provided by AERONET are in reasonable
353 agreement with the results provided by the lidar.

354

355 **Conclusion**

356 In conclusion, this study introduces an approach to partition aerosol mixtures in terms of
357 backscattering coefficients, based on fluorescence and polarization lidar measurements.
358 Specifically, we used the particle depolarization ratio at 532 nm and the fluorescence capacity,
359 allowing for the partitioning of a three-component aerosol mixture at every height/time pixel. The
360 robustness of this approach is demonstrated through testing with Mie-Raman-fluorescence lidar
361 observations at the ATOLL instrumental site, providing valuable insights into the composition and
362 dynamics of atmospheric aerosols. One notable advantage of the proposed approach is its
363 applicability even in conditions of low aerosol content or for aerosol layers in the upper
364 troposphere, where deriving profiles of extinction coefficients might be challenging. Additionally,
365 backscattering coefficients of aerosol components can be converted to particle volume densities
366 using corresponding lidar ratios along with extinction-to-volume conversion factors. While this
367 conversion provides a rough volume estimation, considering the variability of the lidar ratios and
368 the conversion factors within a given aerosol type, a comparison of lidar-derived particle volume
369 during the heatwave over Lille in July 2022 demonstrates promising agreement with AERONET
370 retrievals. At this stage, we have simplified our classification scheme by incorporating four aerosol
371 types: smoke, dust, pollen, and urban particles. It is important to note that the use of fluorescence



372 is an efficient way to distinguish between urban and smoke particles, which is a challenge for other
373 methods that do not utilize fluorescence. However, we recognize the need to expand our approach
374 to include additional aerosol types, particularly those with strong absorption such as polluted urban
375 aerosol. This expansion will involve incorporating additional particle parameters, like lidar ratios,
376 and is planned for our future research. It is crucial to acknowledge that the particle hygroscopic
377 growth complicates the use of fluorescence capacity, resulting in increased uncertainty. To address
378 this, we aim to utilize the additional independent information about aerosol type provided by the
379 fluorescence spectrum. Importantly, the fluorescence spectrum is not affected by relative humidity.
380 In our future research, we plan to further enhance the fluorescence capabilities by increasing the
381 number of fluorescence channels in the lidar.

382

383 **Data availability.** Lidar measurements are available upon request
384 (philippe.goloub@univ-lille.fr).

385

386 **Author contributions.** IV processed the data and wrote the paper. BB prepared the program for
387 aerosol mixture partitioning. QH performed meteorological analysis. TP, GD and WB performed
388 lidar measurements in Lille. PG supervised the project and helped with paper preparation. MK and
389 NK participated in algorithms development and data analysis.

390 .

391 **Competing interests.** The authors declare that they have no conflict of interests.

392

393 **Acknowledgement**

394 We acknowledge funding from the CaPPA project funded by the ANR through the PIA under
395 contract [ANR-11-LABX-0005-01](#), the “Hauts de France” Regional Council (project ECRIN) and
396 the European Regional Development Fund (FEDER). ESA/QA4EO program is greatly
397 acknowledged for supporting the observation activity at LOA. The work from Q. Hu was
398 supported by Agence *Nationale* de Recherche ANR (*ANR-21-ESRE-0013*) through the
399 OBS4CLIM project. Development of algorithms was supported by Russian Science Foundation
400 (project 21-17-00114).

401

402 **References**

403 Ansmann, A., Mamouri, R.-E., Hofer, J., Baars, H., Althausen, D., and Abdullaev, S. F.: Dust
404 mass, cloud condensation nuclei, and ice-nucleating particle profiling with polarization lidar:



- 405 updated POLIPHON conversion factors from global AERONET analysis, *Atmos. Meas. Tech.*,
406 12, 4849–4865, <https://doi.org/10.5194/amt-12-4849-2019>, 2019.
- 407 Ansmann, A., Ohneiser, K., Mamouri, R.-E., Veselovskii, I., Knopf, D. A., Baars, H., Engelmann,
408 R., Foth, A., Jimenez, C., Seifert, P., and Barja, B.: Tropospheric and stratospheric wildfire
409 smoke profiling with lidar: Mass, surface area, CCN and INP retrieval, *Atmos. Chem. Phys.*,
410 21, 9779–9807, <https://doi.org/10.5194/acp-21-9779-2021>, 2021.
- 411 Burton, S. P., Ferrare, R. A., Hostetler, C. A., Hair, J. W., Rogers, R. R., Obland, M. D., Butler, C.
412 F., Cook, A. L., Harper, D. B., and Froyd, K. D.: Aerosol classification using airborne High
413 Spectral Resolution Lidar measurements – methodology and examples, *Atmos. Meas. Tech.*, 5,
414 73–98, <https://doi.org/10.5194/amt-5-73-2012>, 2012.
- 415 Burton, S. P., Ferrare, R. A., Vaughan, M. A., Omar, A. H., Rogers, R. R., Hostetler, C. A., and
416 Hair, J. W.: Aerosol classification from airborne HSRL and comparisons with the CALIPSO
417 vertical feature mask, *Atmos. Meas. Tech.*, 6, 1397–1412, [https://doi.org/10.5194/amt-6-1397-](https://doi.org/10.5194/amt-6-1397-2013)
418 2013, 2013.
- 419 Burton, S. P., Vaughan, M. A., Ferrare, R. A., and Hostetler, C. A.: Separating mixtures of aerosol
420 types in airborne High Spectral Resolution Lidar data, *Atmos. Meas. Tech.*, 7, 419–436,
421 <https://doi.org/10.5194/amt-7-419-2014>, 2014.
- 422 Cao, X., Roy, G., and Bernier, R.: Lidar polarization discrimination of bioaerosols, *Opt. Eng.*, 49,
423 116201, <https://doi.org/10.1117/1.3505877>, 2010.
- 424 Cholleton, D.; Rairoux, P.; Miffre, A.: Laboratory evaluation of the (355, 532) nm particle
425 depolarization ratio of pure pollen at 180.0 lidar backscattering angle. *Remote Sens.* 14, 3767,
426 <https://doi.org/10.3390/rs14153767>, 2022.
- 427 Dubovik, O., Holben, B. N., Eck, T. F., Smirnov, A., Kaufman, Y. J., King, M. D., Tanre, D., and
428 Slutsker, I.: Variability of absorption and optical properties of key aerosol types observed in
429 worldwide locations, *J. Atmos. Sci.*, 59, 590–608, 2002. [https://doi.org/10.1175/1520-](https://doi.org/10.1175/1520-0469(2002)059<0590:voaaop>2.0.co;2)
430 0469(2002)059<0590:voaaop>2.0.co;2
- 431 Floutsi, A. A., Baars, H., Engelmann, R., Althausen, D., Ansmann, A., Bohlmann, S., Heese, B.,
432 Hofer, J., Kanitz, T., Haarig, M., Ohneiser, K., Radenz, M., Seifert, P., Skupin, A., Yin, Z.,
433 Abdullaev, S. F., Komppula, M., Filioglou, M., Giannakaki, E., Stachlewska, I. S., Janicka, L.,
434 Bortoli, D., Marinou, E., Amiridis, V., Gialitaki, A., Mamouri, R.-E., Barja, B., and Wandinger,
435 U.: DeLiAn – a growing collection of depolarization ratio, lidar ratio and Ångström exponent



- 436 for different aerosol types and mixtures from ground-based lidar observations, *Atmos. Meas.*
437 *Tech.*, 16, 2353–2379, <https://doi.org/10.5194/amt-16-2353-2023>, 2023a.
- 438 Floutsi, A. A., Baars, H., and Wandinger, U.: HETEAC-Flex: An optimal estimation method for
439 aerosol typing based on lidar-derived intensive optical properties, *EGUsphere* [preprint],
440 <https://doi.org/10.5194/egusphere-2023-1880>, 2023b.
- 441 Freudenthaler, V., Esselborn, M., Wiegner, M., Heese, B., Tesche, M. and co-authors:
442 Depolarization ratio profiling at several wavelengths in pure Saharan dust during SAMUM
443 2006, *Tellus* 61B, 165–179, doi:10.1111/j.1600-0889.2008.00396.x, 2009.
- 444 Groß, S., Esselborn, M., Weinzierl, B., Wirth, M., Fix, A., and Petzold, A.: Aerosol classification
445 by airborne high spectral resolution lidar observations, *Atmos. Chem. Phys.*, 13, 2487–2505,
446 <https://doi.org/10.5194/acp-13-2487-2013>, 2013.
- 447 Hara, Y., Nishizawa, T., Sugimoto, N., Osada, K., Yumimoto, K., Uno, I., Kudo, R., and Ishimoto,
448 H.: Retrieval of aerosol components using multi-wavelength Mie-Raman lidar and comparison
449 with ground aerosol sampling, *Remote Sens.*, 10, 937, 2018. <https://doi.org/10.3390/rs10060937>
- 450 He, Y., Yin, Z., Ansmann, A., Liu, F., Wang, L., Jing, D., and Shen, H.: POLIPHON conversion
451 factors for retrieving dust-related cloud condensation nuclei and ice-nucleating particle
452 concentration profiles at oceanic sites, *Atmos. Meas. Tech.*, 16, 1951–1970,
453 <https://doi.org/10.5194/amt-16-1951-2023>, 2023.
- 454 Mamouri, R.-E., and Ansmann, A.: Potential of polarization/Raman lidar to separate fine dust,
455 coarse dust, maritime, and anthropogenic aerosol profiles, *Atmos. Meas. Tech.*, 10, 3403–3427,
456 <https://doi.org/10.5194/amt-10-3403-2017>, 2017.
- 457 Miffre, A., Cholleton, D., and Rairoux, P.: On the use of light polarization to investigate the size,
458 shape, and refractive index dependence of backscattering Ångström exponents, *Opt. Lett.* 45,
459 1084–1087, <https://doi.org/10.1364/OL.385107>, 2020.
- 460 Mylonaki, M., Giannakaki, E., Papayannis, A., Papanikolaou, C.-A., Komppula, M., Nicolae, D.,
461 Papagiannopoulos, N., Amodeo, A., Baars, H., and Soudiana, O.: Aerosol type classification
462 analysis using EARLINET multiwavelength and depolarization lidar observations, *Atmos.*
463 *Chem. Phys.*, 21, 2211–2227, <https://doi.org/10.5194/acp-21-2211-2021>, 2021.
- 464 Nicolae, D., Vasilescu, J., Talianu, C., Binietoglou, I., Nicolae, V., Andrei, S., and Antonescu, B.:
465 A neural network aerosol-typing algorithm based on lidar data, *Atmos. Chem. Phys.*, 18,
466 14511–14537, <https://doi.org/10.5194/acp-18-14511-2018>, 2018.



- 467 Papagiannopoulos, N., Mona, L., Amodeo, A., D'Amico, G., Gumà Claramunt, P., Pappalardo, G.,
468 Alados-Arboledas, L., Guerrero-Rascado, J. L., Amiridis, V., Kokkalis, P., Apituley, A., Baars,
469 H., Schwarz, A., Wandinger, U., Binietoglou, I., Nicolae, D., Bortoli, D., Comerón, A.,
470 Rodríguez-Gómez, A., Sicard, M., Papayannis, A., and Wiegner, M.: An automatic observation-
471 based aerosol typing method for EARLINET, *Atmos. Chem. Phys.*, 18, 15879–15901,
472 <https://doi.org/10.5194/acp-18-15879-2018>, 2018.
- 473 Reichardt, J., Leinweber, R., Schwebe, A.: Fluorescing aerosols and clouds: investigations of co-
474 existence, *EPJ Web Conf.*, 176, 05010, <https://doi.org/10.1051/epjconf/201817605010>, 2018.
- 475 Reichardt, J., Behrendt, O., and Lauer mann, F.: Spectrometric fluorescence and Raman lidar:
476 absolute calibration of aerosol fluorescence spectra and fluorescence correction of humidity
477 measurements, *Atmos. Meas. Tech.*, 16, 1–13, <https://doi.org/10.5194/amt-16-1-2023>, 2023.
- 478 Stein, A. F., Draxler, R. R., Rolph, G. D., Stunder, B. J. B., Cohen, M. D., and Ngan, F.: NOAA's
479 HYSPLIT atmospheric transport and dispersion modeling system, *B. Am. Meteorol. Soc.*, 96,
480 2059–2077, <https://doi.org/10.1175/BAMS-D-14-00110.1>, 2015.
- 481 Sugimoto, N. and Lee, C. H.: Characteristics of dust aerosols inferred from lidar depolarization
482 measurements at two wavelengths, *Appl. Optics*, 45, 7468–7474,
483 <https://doi.org/10.1364/AO.45.007468>, 2006.
- 484 Tesche, M., Ansmann, A., Müller, D., Althausen, D., Engelmann, R., Freudenthaler, V., and Groß,
485 S.: Vertically resolved separation of dust and smoke over Cape Verde using multiwavelength
486 Raman and polarization lidars during Saharan Mineral Dust Experiment 2008, *J. Geophys. Res.*,
487 114, D13202, doi:10.1029/2009JD011862, 2009.
- 488 Veselovskii, I., Hu, Q., Goloub, P., Podvin, T., Korenskiy, M., Pujol, O., Dubovik, O., Lopatin,
489 A.: Combined use of Mie-Raman and fluorescence lidar observations for improving aerosol
490 characterization: feasibility experiment, *Atm. Meas. Tech.*, 13, 6691–6701,
491 doi.org/10.5194/amt-13-6691-2020, 2020.
- 492 Veselovskii, I., Hu, Q., Goloub, P., Podvin, T., Choël, M., Visez, N., and Korenskiy, M.: Mie-
493 Raman-fluorescence lidar observations of aerosols during pollen season in the north of France,
494 *Atm. Meas. Tech.*, 14, 4773–4786, doi.org/10.5194/amt-14-4773-2021, 2021.
- 495 Veselovskii, I., Hu, Q., Goloub, P., Podvin, T., Barchunov, B., and Korenskiy, M.: Combining
496 Mie-Raman and fluorescence observations: a step forward in aerosol classification with lidar



497 technology, *Atmos. Meas. Tech.*, 15, 4881–4900, <https://doi.org/10.5194/amt-15-4881-2022>,
498 2022.

499 Veselovskii, I., Hu, Q., Goloub, P., Podvin, T., Boissiere, W., Korenskiy, M., Kasianik, N.,
500 Khaykin, S., and Miri, R.: Derivation of aerosol fluorescence and water vapor Raman
501 depolarization ratios from lidar measurements, *Atmos. Meas. Tech. Discuss.* [preprint],
502 <https://doi.org/10.5194/amt-2023-210>, 2023.

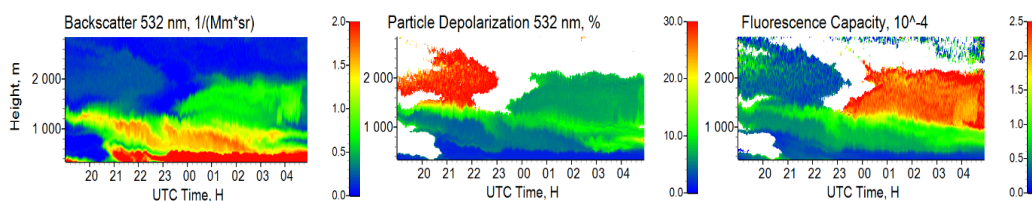
503 Voudouri, K. A., Siomos, N., Michailidis, K., Papagiannopoulos, N., Mona, L., Cornacchia, C.,
504 Nicolae, D., and Balis, D.: Comparison of two automated aerosol typing methods and their
505 application to an EARLINET station, *Atmos. Chem. Phys.*, 19, 10961–10980,
506 <https://doi.org/10.5194/acp-19-10961-2019>, 2019.

507 Zhang, Y., Sun, Z., Chen, S., Chen, H., Guo, P., Chen, S., He, J., Wang, J., Nian, X.: Classification
508 and source analysis of low-altitude aerosols in Beijing using fluorescence–Mie polarization
509 lidar, *Optics Communications*, 479, 126417, <https://doi.org/10.1016/j.optcom.2020.126417>,
510 2021.

511 Wandinger, U., Floutsi, A. A., Baars, H., Haarig, M., Ansmann, A., Hünerbein, A., Docter, N.,
512 Donovan, D., van Zadelhoff, G.-J., Mason, S., and Cole, J.: HETEAC – the Hybrid End-To-
513 End Aerosol Classification model for EarthCARE, *Atmos. Meas. Tech.*, 16, 2485–2510,
514 <https://doi.org/10.5194/amt-16-2485-2023>, 2023.

515 Wang, N., Shen, X., Xiao, D., Veselovskii, I., Zhao, C., Chen, F., Liu, C., Rong, Y., Ke, J., Wang,
516 B., Qi, B., Liu, D.: Development of ZJU high-spectral-resolution lidar for aerosol and cloud:
517 feature detection and classification, *Journal of Quantitative Spectroscopy & Radiative Transfer*,
518 v.261, 107513, doi.org/10.1016/j.jqsrt.2021.107513, 2021.

519



520

521 Fig.1. Spatiotemporal distributions of the backscattering coefficient at 532 nm, particle
 522 depolarization ratio at 532 nm and fluorescence capacity during the night of March 27-28, 2022.

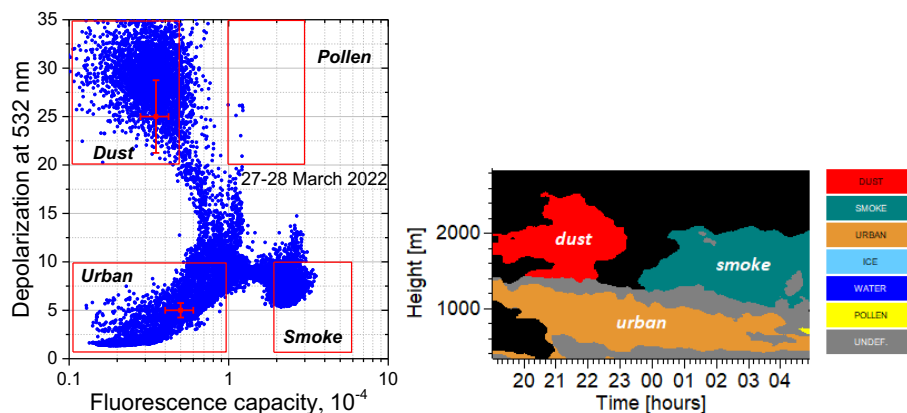
523 The depolarization ratio and fluorescence capacity are calculated only for the values $\beta_{532} > 0.1 \text{ Mm}^{-1}$
 524 sr^{-1} . The measurements were taken at an angle of 45° to the horizon.

525

526

527

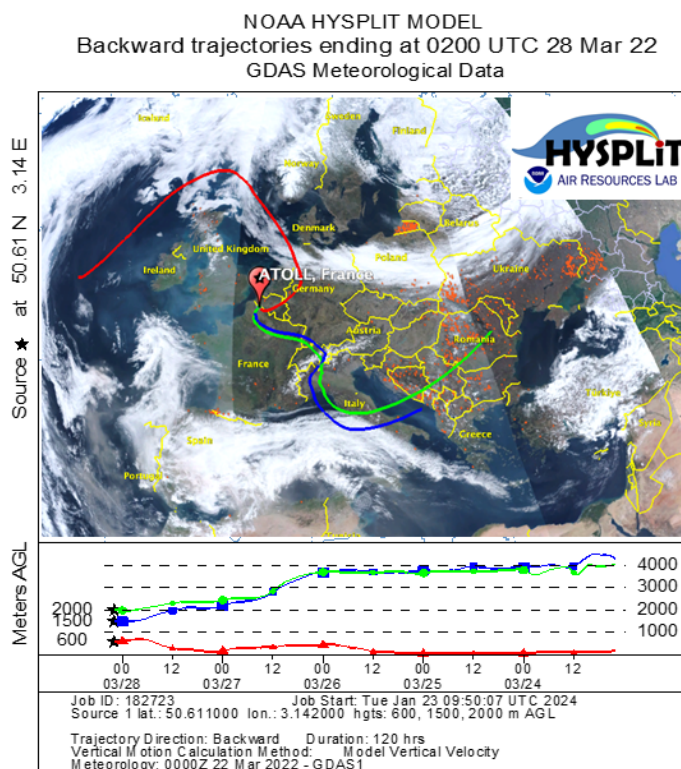
528



529

530 Fig.2. (a) The $\delta_{532}-G_F$ diagram for observations in the height range of 3500 m–2800 m and (b) the
 531 spatiotemporal distribution of aerosol types during the night of March 27–28, 2022.

532



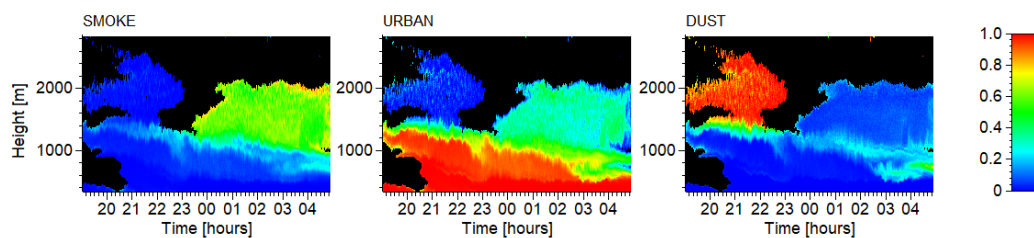
533

534 Fig.3. The HYSPLIT five-day backward trajectories for the air mass over Lille at altitudes 600 m,
 535 1500 m, and 2000 m on March 28, 2022 at 02:00 UTC. Red dots depict the regions of forest fires.

536

537

538



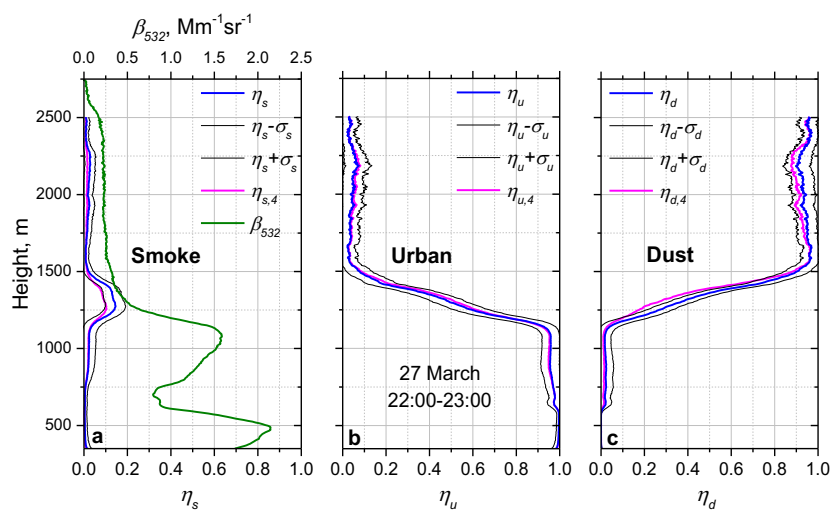
539

540 Fig.4. Relative contributions of smoke (η_s), urban (η_u), and dust (η_d) particles to the backscattering
 541 coefficient β_{532} during the night of March 27–28, 2022.

542



543



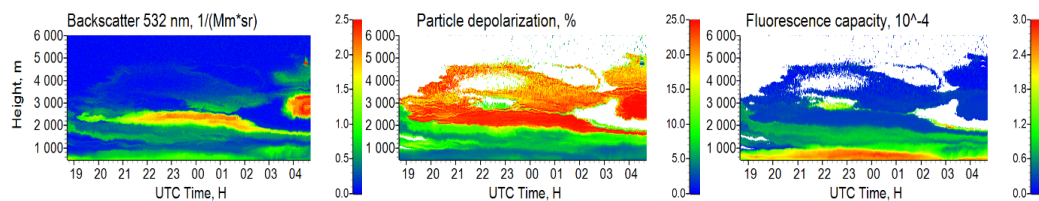
544

545 Fig.5. Vertical profiles of the relative contributions of smoke (η_s), urban (η_u), and dust (η_d) particles
546 to the backscattering coefficient β_{532} on March 27, 2022. These profiles are derived under the
547 assumption that only three aerosol types occur. The black lines depict the deviation of solutions
548 from the mean value ($\eta_i \pm \sigma_i$). Magenta lines show the relative contributions of smoke, urban and
549 dust particles ($\eta_{s,4}$, $\eta_{u,4}$, $\eta_{d,4}$) when four aerosol types (including pollen) are considered.

550



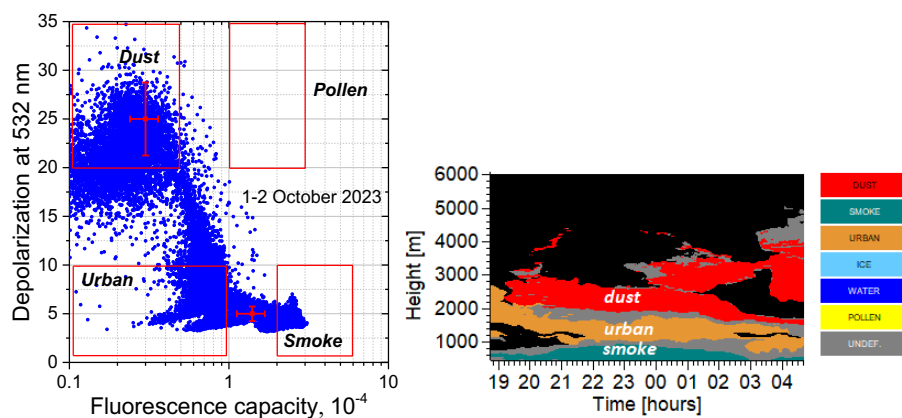
551



552

553 Fig.6. Spatiotemporal distributions of the backscattering coefficient at 532 nm, particle
554 depolarization ratio at 532 nm and fluorescence capacity during the night of October 1-2, 2023.
555 The depolarization ratio and fluorescence capacity are calculated only for values of $\beta_{532} > 0.1 \text{ Mm}^{-2}$
556 sr^{-1} .

557



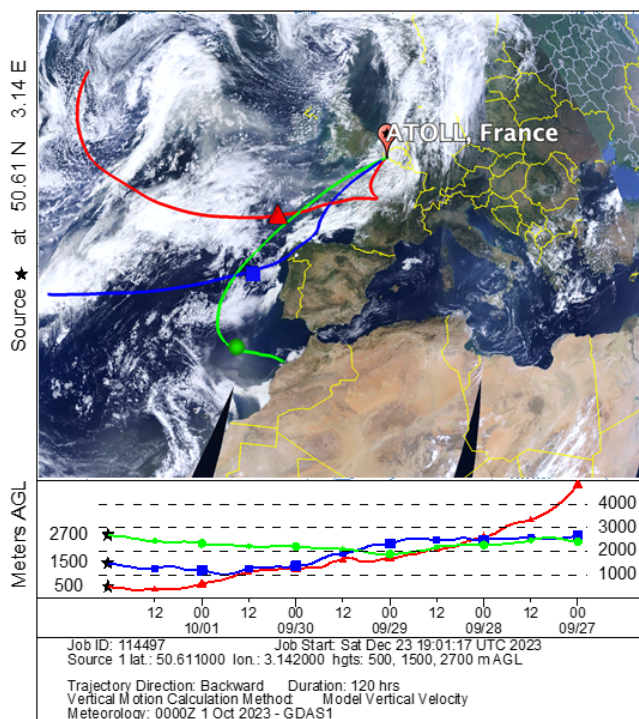
558

559 Fig.7. (a) The $\delta_{532}-G_F$ diagram and (b) the spatiotemporal distribution of aerosol types during the
560 night of October 1-2, 2023.

561



NOAA HYSPLIT MODEL
Backward trajectories ending at 0000 UTC 02 Oct 23
GDAS Meteorological Data



562

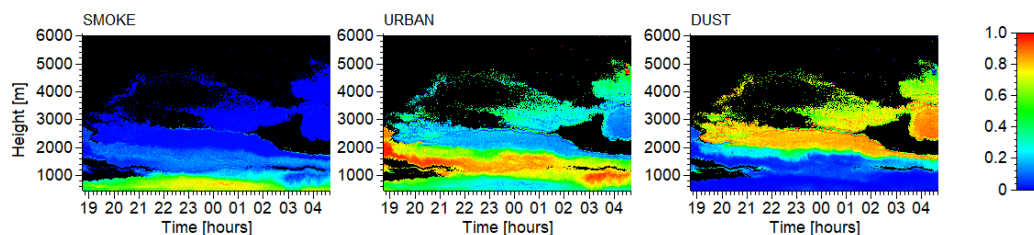
563 Fig.8. The HYSPLIT five-day backward trajectories for the air mass over Lille at altitudes 500 m,

564 1500 m, and 2700 m on October 2, 2023 at 00:00 UTC.

565



566



567

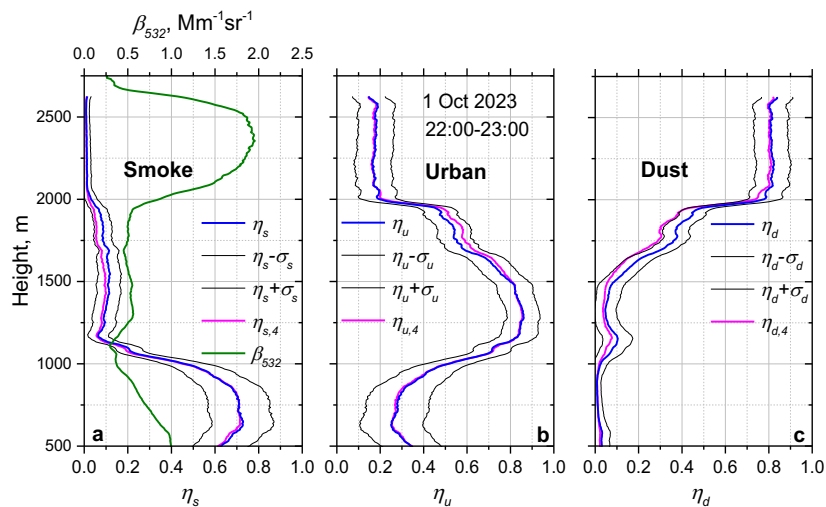
568 Fig.9. The relative contributions of smoke (η_s), urban (η_u), and dust (η_d) particles to the
 569 backscattering coefficient β_{532} during the night of October 1-2, 2023.

570

571

572

573

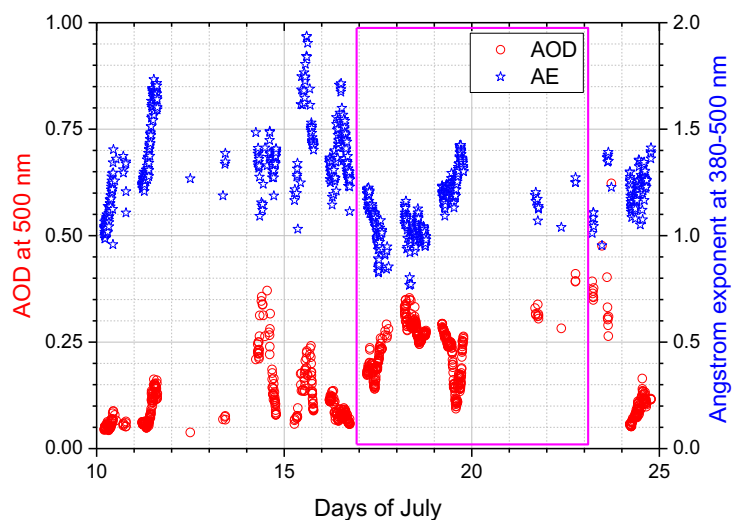


574

575 Fig.10. Vertical profiles of the relative contributions of smoke (η_s), urban (η_u), and dust (η_d)
 576 particles to the backscattering coefficient β_{532} on October 1, 2023. The profiles are derived under
 577 the assumption that only three aerosol types occur. The black lines depict the deviation of solutions
 578 from the mean value ($\eta_i \pm \sigma_i$). The magenta lines show the relative contributions of smoke, dust and
 579 urban particles ($\eta_{s,4}$, $\eta_{u,4}$, $\eta_{d,4}$) when four aerosol types (including pollen) are considered.

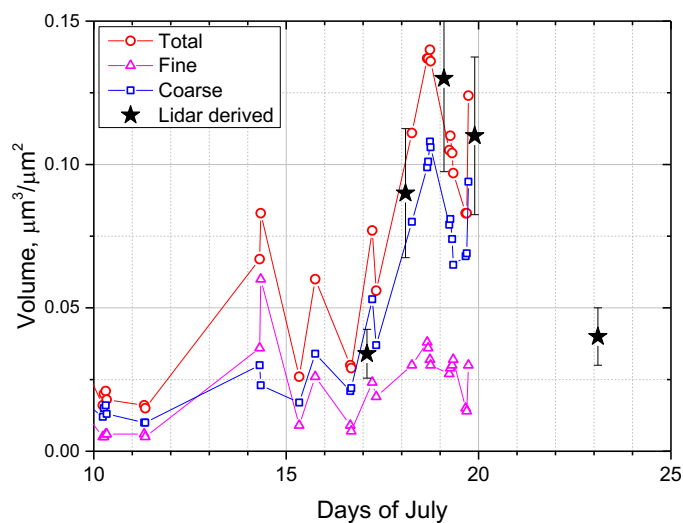
580

581



582

583 Fig.11. The aerosol optical depth (AOD) at 500 nm and the Angstrom exponent (AE) provided by
584 AERONET over Lille in July 2022. Magenta box depicts the time period during which lidar
585 observations in this study were analyzed.



586

587 Fig.12. Column-integrated aerosol volume (circles) in July 2022 provided by AERONET. The
588 triangles and squares represent the volumes of the fine and coarse modes, respectively. Black stars
589 depict the particle volume derived from lidar observations.

590

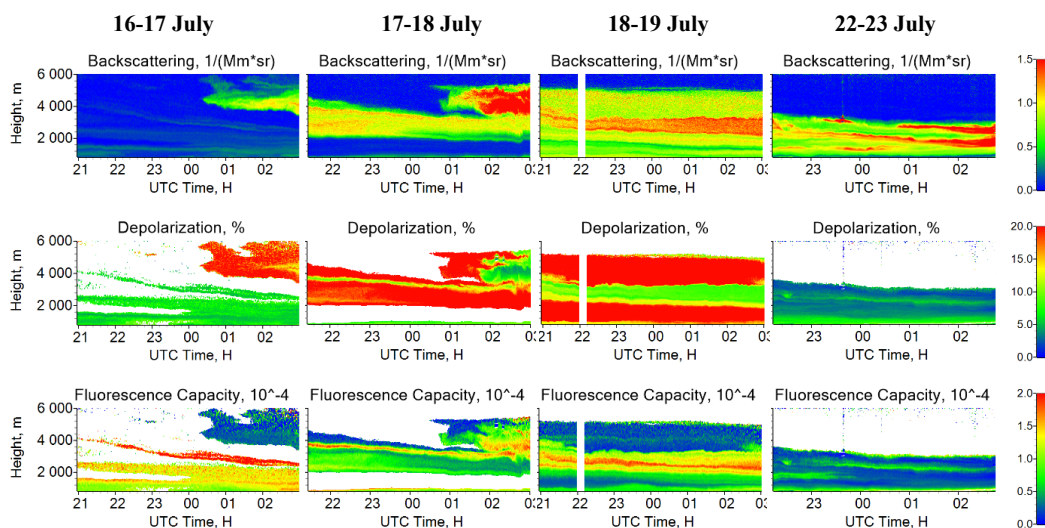


591

592

593

594



595

596

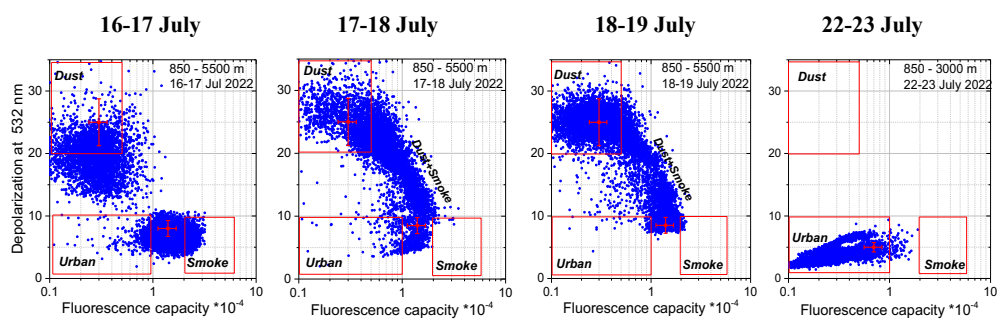
597

598 Fig.13. Spatiotemporal distributions of the backscattering coefficient β_{532} , the particle
599 depolarization ratio δ_{532} , and the fluorescence capacity G_F for the nights of July 16-17, 17-18, 18-
600 19 and 22-23, 2022. The depolarization ratio and fluorescence capacity are calculated only for the
601 values $\beta_{532} > 0.1 Mm^{-1}sr^{-1}$.
602

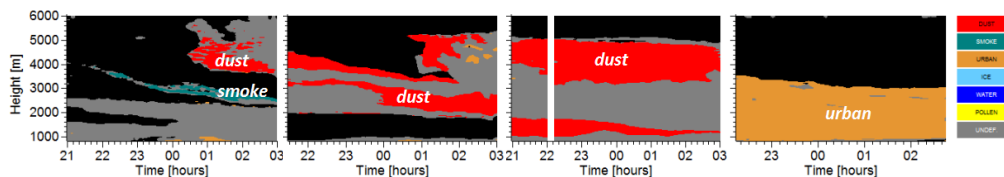


603

604



605



606

607 Fig.14. The $\delta_{532}-G_F$ diagram (upper row) and the spatiotemporal distribution of aerosol types

608 (bottom row) for the measurements for the nights of July 16-17, 17-18, 18-19 and 22-23, 2022.

609 The grey coloring represents an undefined aerosol type.

610

611



612

613

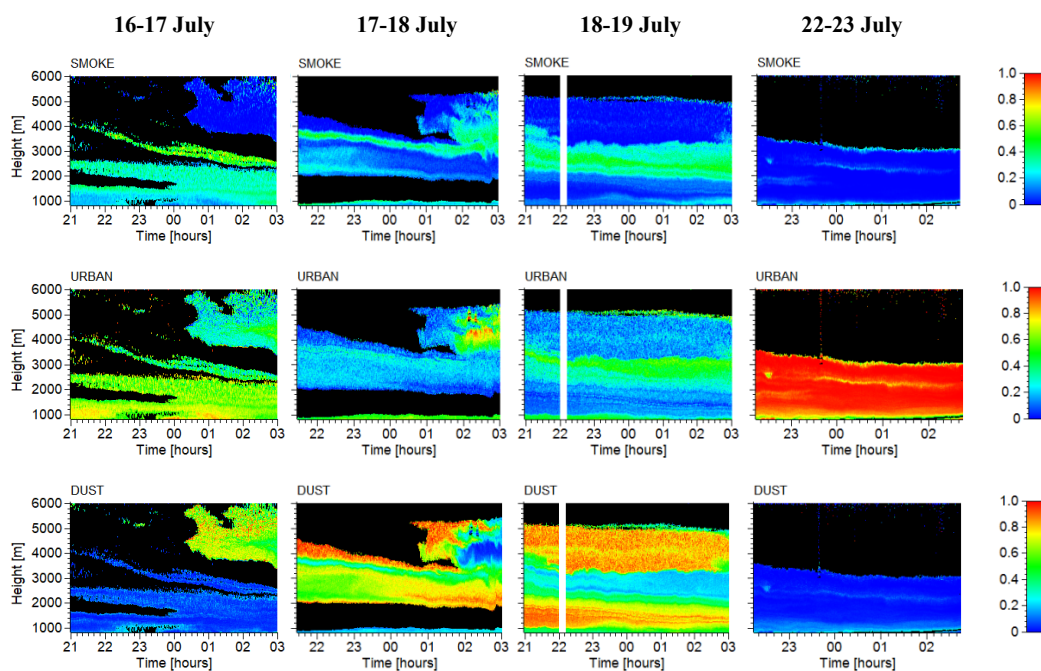
614

615

616

617 Fig.15. The relative contributions of smoke, urban and dust particles to the backscattering
618 coefficient at 532 nm for the nights of July 16-17, 17-18, 18-19 and 22-23, 2022.

619





620

621

622

623

624

625

626

627

628

629

630

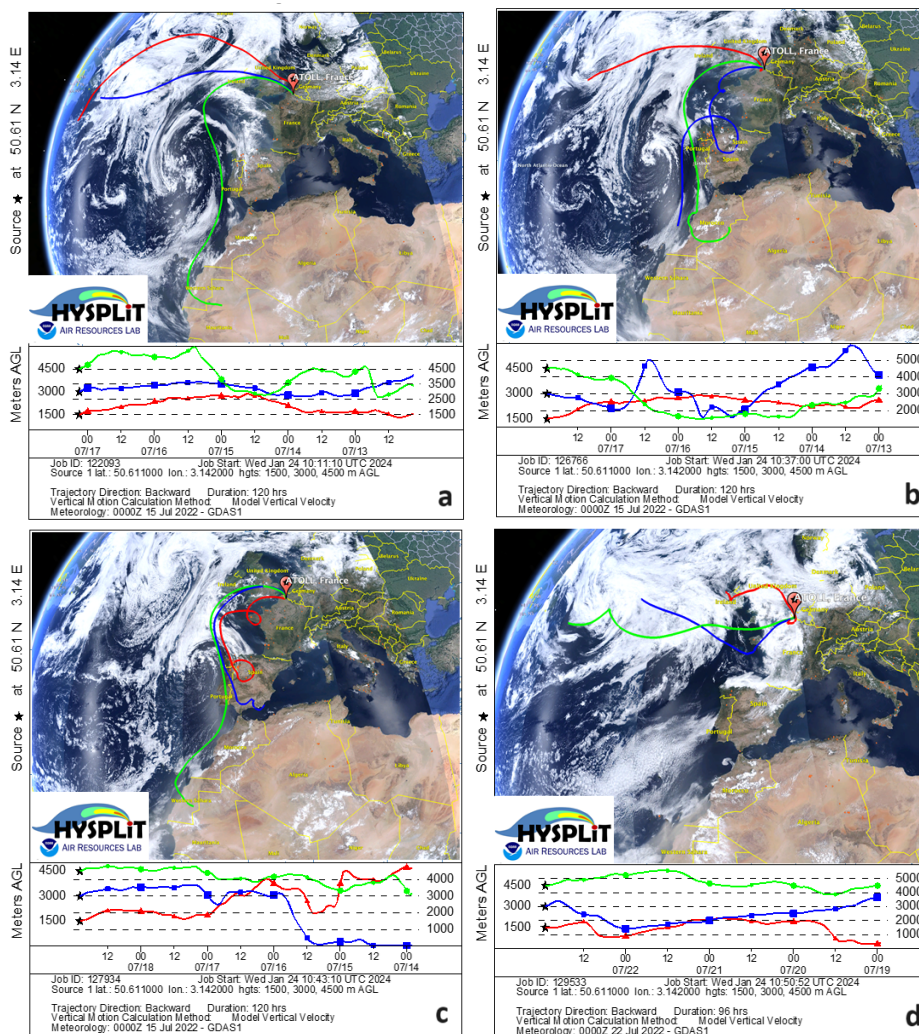
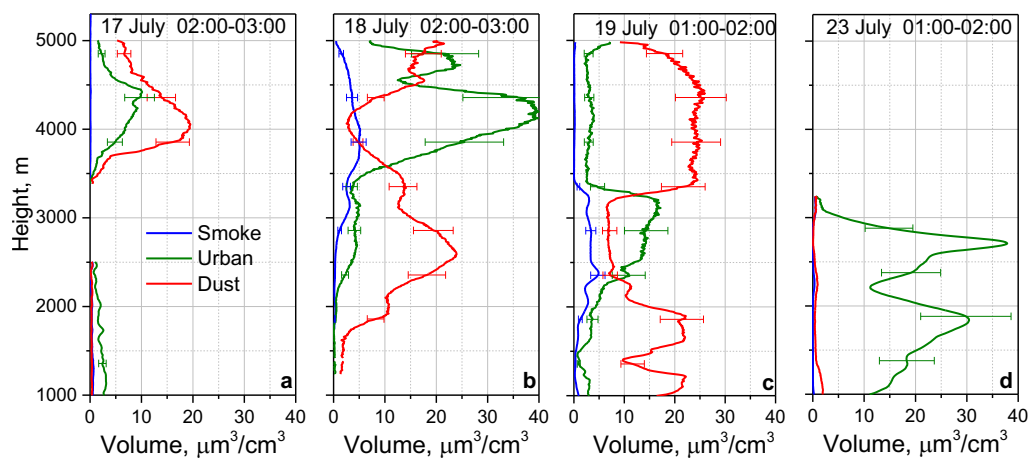


Fig.16. The HYSPLIT five-day backward trajectories for the air mass over Lille at altitudes 1500 m, 3000 m, and 4500 m on (a) July 17, 2022 at 03:00 UTC; (b) July 17, 2022 at 23:00 UTC; (c) July 18, 2022 at 22:00 UTC; (d) July 22, 2022 at 22:00 UTC. Red dots depict the regions of forest fires.



631

632 Fig.17. Vertical profiles of the volume density of smoke, dust and urban particles derived from η_s ,

633 η_u , and η_d presented in Fig.13, using the mean values of the lidar ratios and the conversion factors

634 from Table 2.

635